

# High-efficiency oxygen reduction to hydrogen peroxide catalysed by oxidized carbon materials

Zhiyi Lu<sup>1</sup>, Guangxu Chen<sup>1</sup>, Samira Siahrostami<sup>2</sup>, Zhihua Chen<sup>3</sup>, Kai Liu<sup>1</sup>, Jin Xie<sup>1</sup>, Lei Liao<sup>1</sup>, Tong Wu<sup>1</sup>, Dingchang Lin<sup>1</sup>, Yayuan Liu<sup>1</sup>, Thomas F. Jaramillo<sup>3</sup>, Jens K. Nørskov<sup>2,4</sup> and Yi Cui<sup>1,5\*</sup>

**Hydrogen peroxide (H<sub>2</sub>O<sub>2</sub>) is a valuable chemical with a wide range of applications, but the current industrial synthesis of H<sub>2</sub>O<sub>2</sub> involves an energy-intensive anthraquinone process. The electrochemical synthesis of H<sub>2</sub>O<sub>2</sub> from oxygen reduction offers an alternative route for on-site applications; the efficiency of this process depends greatly on identifying cost-effective catalysts with high activity and selectivity. Here, we demonstrate a facile and general approach to catalyst development via the surface oxidation of abundant carbon materials to significantly enhance both the activity and selectivity (~90%) for H<sub>2</sub>O<sub>2</sub> production by electrochemical oxygen reduction. We find that both the activity and selectivity are positively correlated with the oxygen content of the catalysts. The density functional theory calculations demonstrate that the carbon atoms adjacent to several oxygen functional groups (–COOH and C–O–C) are the active sites for oxygen reduction reaction via the two-electron pathway, which are further supported by a series of control experiments.**

The enormous need for hydrogen peroxide (H<sub>2</sub>O<sub>2</sub>) places this chemical as one of the 100 most important chemicals in the world<sup>1</sup>. H<sub>2</sub>O<sub>2</sub> is a potential energy carrier<sup>2</sup> and an environmentally friendly oxidant for various chemical industries and environmental remediation<sup>3</sup>, thus the need for efficient and inexpensive H<sub>2</sub>O<sub>2</sub> production is essential. The current industrial process for the synthesis of H<sub>2</sub>O<sub>2</sub> involves an energy-intensive anthraquinone oxidation/reduction, which requires complex and large-scale infrastructure and generates a substantial volume of waste chemicals<sup>3</sup>. The direct synthesis of H<sub>2</sub>O<sub>2</sub> from hydrogen and oxygen in the presence of catalysts<sup>4–6</sup> provides a more straightforward route and ideally solves the issues associated with the indirect anthraquinone route. However, as the hydrogen/oxygen mixture is potentially explosive, researchers have aimed to eliminate the danger of explosion and to simultaneously find selective and active catalysts<sup>4,7–10</sup>. Another attractive and alternative route for the on-site direct production of H<sub>2</sub>O<sub>2</sub> is through an electrochemical process in a fuel cell setup, where oxygen reduction undergoes a two-electron pathway<sup>11–13</sup>. Substantial efforts in recent years on this fuel cell concept have aimed at efficiently generating electricity simultaneously with a high-yield production of H<sub>2</sub>O<sub>2</sub> (refs<sup>14–20</sup>).

For the two-electron route, electrocatalysts with high activity and selectivity are a prerequisite. Noble metals and their alloys (for example, Pd–Au<sup>21</sup>, Pt–Hg<sup>14</sup> and Pd–Hg<sup>15</sup>) are currently the most efficient catalysts, requiring small overpotentials for oxygen reduction as well as high H<sub>2</sub>O<sub>2</sub> selectivity (up to ~98%). However, the scarcity of noble metals may hinder their large-scale application. Carbon-based materials have shown great promise as alternative catalysts for the electrochemical synthesis of H<sub>2</sub>O<sub>2</sub>, as they are earth-abundant, highly tunable and electrochemically stable under reaction conditions. Recent studies demonstrate the capability of carbon materials for the electrochemical production of H<sub>2</sub>O<sub>2</sub>, with their performance strongly correlated to heteroatom doping<sup>16,22–24</sup> and material structure<sup>18,25–27</sup>, as both of these parameters can tailor

the electronic structure of carbon atoms. Despite progress in this area, there is room for improvement in developing improved carbon-based materials, and much to learn regarding structure–activity relationships.

Herein, we demonstrate an effective approach to enhancing both the activity and selectivity of carbon materials for H<sub>2</sub>O<sub>2</sub> production by means of surface oxidation of the carbon catalyst. For example, after oxidizing commercially available carbon nanotubes (CNTs), we observe a significant decrease in overpotential and an enhanced selectivity up to ~90% in both basic and neutral media. Catalyst characterization reveals the existence of both C–O and C=O functional groups on the surface of the oxidized CNTs (O-CNTs). The oxygen reduction reaction (ORR) activity and selectivity are found to be positively correlated with the oxygen content, indicating the importance of oxygen functional groups. The general efficacy of this approach is demonstrated by observing a similarly enhanced oxygen reduction performance on other forms of oxidized carbon—oxidized super P (O-SP) and oxidized acetylene black (O-AB)—which have a much lower cost than O-CNT. To elucidate the catalytic mechanism, we employ density functional theory (DFT) calculations to investigate the activities of a wide variety of oxygen functional groups and identify several possible sites with enhanced ORR activity. Moreover, guided by the DFT results, a series of experiments are performed to fabricate O-CNTs with prominent selectivity, which further supports the active sites of the oxidized carbon materials for electrochemical H<sub>2</sub>O<sub>2</sub> synthesis.

## Results

**ORR activities of CNTs and O-CNTs.** The O-CNTs were prepared by the chemical oxidation of CNTs using concentrated nitrate acid (see Methods for more details)<sup>28</sup>. The ORR performance was evaluated in an aqueous solution (0.1 M KOH or 0.1 M phosphate buffered saline) using a rotating ring-disk electrode. The ORR can follow either of a 4e<sup>−</sup> or 2e<sup>−</sup> pathway. The 2e<sup>−</sup> pathway is preferred

<sup>1</sup>Department of Material Science and Engineering, Stanford University, Stanford, CA, USA. <sup>2</sup>SUNCAT Center for Interface Science and Catalysis, Department of Chemical Engineering, Stanford University, Stanford, CA, USA. <sup>3</sup>Department of Chemical Engineering, Stanford University, Stanford, CA, USA. <sup>4</sup>SLAC National Accelerator Laboratory, Menlo Park, CA, USA. <sup>5</sup>Stanford Institute for Materials and Energy Science, SLAC National Accelerator Laboratory, Menlo Park, CA, USA. Zhiyi Lu, Guangxu Chen and Samira Siahrostami contributed equally to this work. \*e-mail: [yicui@stanford.edu](mailto:yicui@stanford.edu)

in this study as the production of  $\text{H}_2\text{O}_2$  is the objective. Figure 1a shows electrochemical results in a basic electrolyte (0.1 M KOH, pH ~13), the oxygen reduction currents measured on a disk electrode (solid lines) and the  $\text{H}_2\text{O}_2$  oxidation currents measured on a platinumium ring electrode (dashed lines). The amount of  $\text{H}_2\text{O}_2$  formed was quantified by the ring electrode, which was potentiostated at 1.2 V (versus the reversible hydrogen electrode, the same below) to avoid ORR currents at the ring, allowing only  $\text{H}_2\text{O}_2$  oxidation. According to the polarization curves, the O-CNTs showed a much higher current and a remarkably lower overpotential (~130 mV lower at 0.2 mA) with respect to the commercial CNTs. It should be noted that the current increased very quickly to the limiting current for the O-CNTs, indicating fast ORR kinetics, which was also reflected in the lower Tafel slope (Supplementary Fig. 1)<sup>29</sup>. This fast kinetics may make the O-CNTs a promising candidate in alkaline fuel cells for the synthesis of  $\text{H}_2\text{O}_2$ . In addition to the higher activity, the O-CNTs exhibited a significantly higher  $\text{H}_2\text{O}_2$  selectivity (around ~90% in the potential range of 0.4–0.65 V) than the CNTs (~60%), as shown in Fig. 1c. This performance enhancement was also observed in neutral electrolyte (pH ~7), where the onset potential measured at 0.05 mA shifted in a positive direction by ~150 mV and the selectivity increased from ~60% to ~85% for CNTs exposed to the oxidation treatment (Fig. 1b,d). The stability of the O-CNTs was demonstrated by long-term testing (~10 h) with negligible changes in activity or selectivity as measured on both the

ring and disc electrodes (Fig. 1e,f). The gradual degradation on the ring current in neutral electrolyte was attributed to anion poisoning rather than current efficiency degradation, as the ring current could be recovered after electrochemical ring cleaning. The ORR activity of the O-CNTs was also evaluated under acidic conditions (0.1 M  $\text{HClO}_4$ ), as shown in Supplementary Fig. 2. It is observed that the activity and selectivity are both significantly improved compared with CNTs, but not as good as those performed under base conditions.

The high activity and selectivity of the O-CNT catalyst make it the most active non-precious electrocatalyst towards electrochemical reduction of oxygen to  $\text{H}_2\text{O}_2$  under basic conditions (Supplementary Table 1)<sup>22,24,30,31</sup>. To improve the ORR current for practical applications, we loaded our catalyst onto Teflon-treated carbon fibre paper with a loading of ~0.5  $\text{mg cm}^{-2}$  and measured their steady-state polarization curves (Supplementary Fig. 3). The Teflon-treated carbon fibre paper is highly hydrophobic, thus providing abundant three-phase contact points for the ORR<sup>32,33</sup>. In 1 M KOH, the electrode achieved current densities of 20 and 40  $\text{mA cm}^{-2}$  at 0.72 and 0.68 V, respectively, while maintaining a similarly high selectivity of >90%. In addition, we performed the ORR performance of O-CNT catalysts in a reactor reported previously<sup>20</sup> and it was found that the  $\text{H}_2\text{O}_2$  concentration can be easily accumulated to around 1,975  $\text{mg l}^{-1}$  within 30 min (the polarization curve and  $V-t$  curve under constant current of the reactor can be

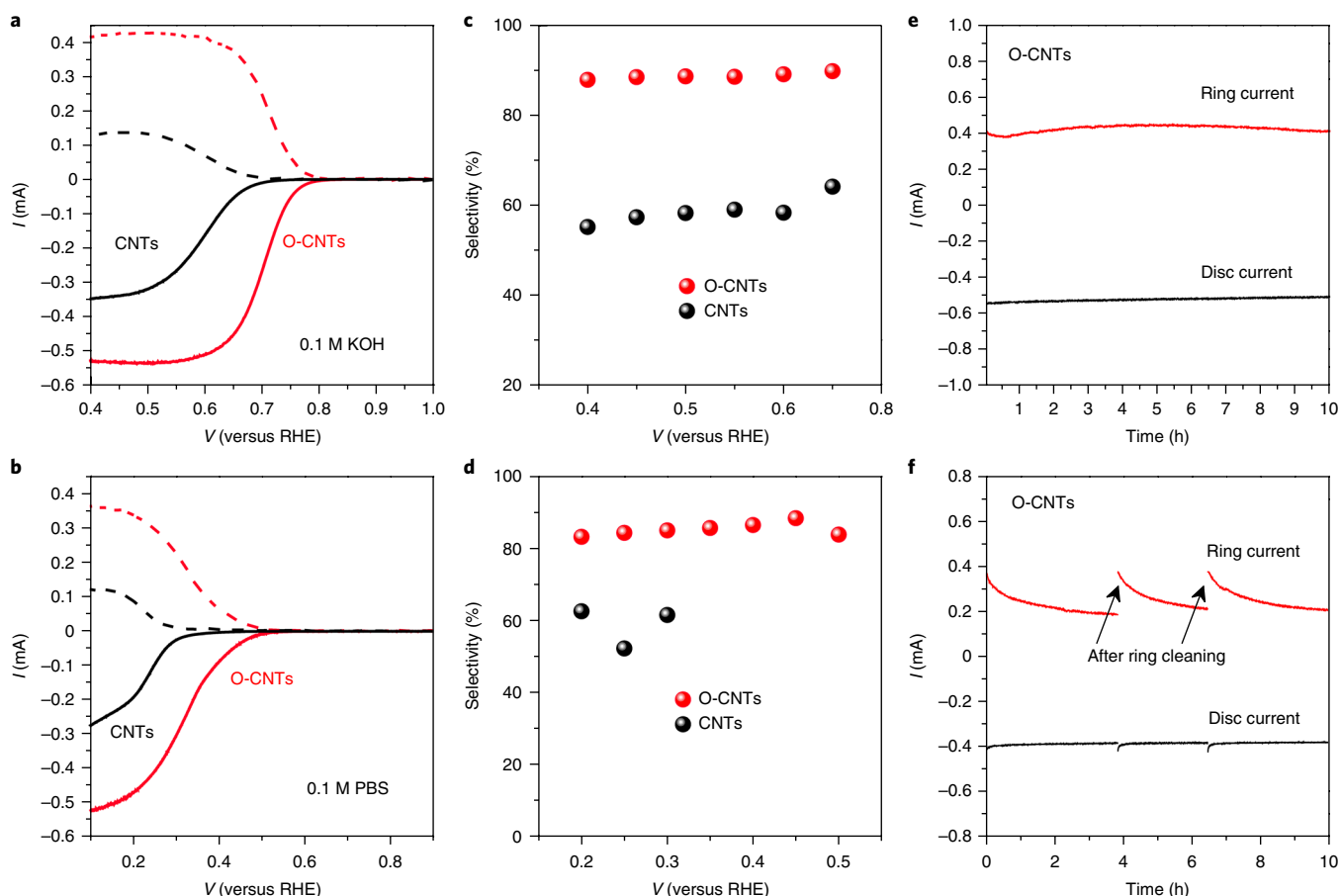


**Fig. 1 | Oxygen reduction performance of CNTs and O-CNTs.** **a, b**, Polarization curves at 1,600 r.p.m. (solid lines) and simultaneous  $\text{H}_2\text{O}_2$  detection currents at the ring electrode (dashed lines) for both catalysts in 0.1 M KOH (**a**) or 0.1 M phosphate buffered saline (PBS; **b**). **c, d**, Calculated selectivity of these two catalysts at various potentials at 0.1 M KOH (**c**) and 0.1 M PBS (**d**). **e, f**, Stability measurements of O-CNTs at 0.1 M KOH (**e**) and 0.1 M PBS (**f**). These results indicate that the O-CNTs possess both higher activity and higher  $\text{H}_2\text{O}_2$  selectivity than CNTs towards oxygen reduction to produce  $\text{H}_2\text{O}_2$  in alkaline and neutral electrolytes. RHE, reversible hydrogen electrode.

seen in Supplementary Fig. 4). Compared with previous reports (Supplementary Table 2)<sup>16,25,26</sup>, the yield and production rate are still among the highest values, demonstrating that electrochemical reduction of oxygen to H<sub>2</sub>O<sub>2</sub> is practical in an alkali environment.

**Characterizations of CNTs and O-CNTs.** Physical and chemical characterization of the two samples may shed light on the origin of the performance enhancement. Transmission electron microscopy images (Fig. 2a,b) and X-ray diffraction patterns (Fig. 2c) demonstrate that the tube-like structure and crystallinity were not affected by the oxidation process. Raman spectra of both samples (Fig. 2d) reveal that the intensity ratio of the D and G peaks was slightly increased after oxidation, indicating that the oxidation process created some disorder (that is, defect) in the graphitic structure<sup>28</sup>. Figure 2e depicts the X-ray photoelectron spectroscopy (XPS) survey scans to detect the elements presented on the CNT and O-CNT surfaces. A new peak that can be indexed to oxygen 1s emerged after nitric acid treatment, yielding a carbon-to-oxygen ratio of 92:8, which is substantially different from the commercial CNTs that exhibited negligible oxygen content. The carbon 1s spectrum of the O-CNTs (Fig. 2f) can be deconvoluted into the following bands: carbon in graphite at 284.5 eV, defects (attributed to carbon atoms no longer in the regular tubular structure) at 285.4 eV, carbon singly bound to oxygen (C–O) at 286.1 eV, carbon bound to two oxygens

(that is, –COOH) at 288.7 eV and the characteristic shakeup line of carbon in aromatic compounds at 290.5 eV ( $\pi$ – $\pi^*$  transition)<sup>34</sup>. The deconvolution of the oxygen 1s spectrum (Fig. 2g) shows two peaks: oxygen doubly bound to carbon (C=O) at 531.6 eV and oxygen singly bound to carbon (C–O) at 533.2 eV<sup>35</sup>. These results indicate that the oxidation treatment induced more oxygen-containing functional groups (for example, C–OH, C–O–C, C=O and C–OOH, which is confirmed by the Fourier-transform infrared spectroscopy spectrum in Supplementary Fig. 5), accompanied with a slightly more disordered structure for the O-CNTs.

Additional control experiments were performed to identify the main reason for enhanced performance. The commercial CNTs usually incorporate iron-based catalysts<sup>36,37</sup>, which may contribute to the ORR activity and selectivity. Thus, we determined the iron concentrations of the catalysts by inductively coupled plasma mass spectrometry, as listed in Supplementary Table 3. The results demonstrated that the iron in CNTs can be removed by the oxidation treatment. They also showed that the iron concentration in commercial carbon nanoparticles (for example, super P (SP)) is one magnitude less than in CNTs. However, as the ORR activity and selectivity of SP that is free of iron are both similar to those of CNTs (shown next), we believe that the small amount of iron in CNTs may not play a vital role in determining the ORR performance. Moreover, in terms of the trace amount of iron in SP and O-SP and the greatly

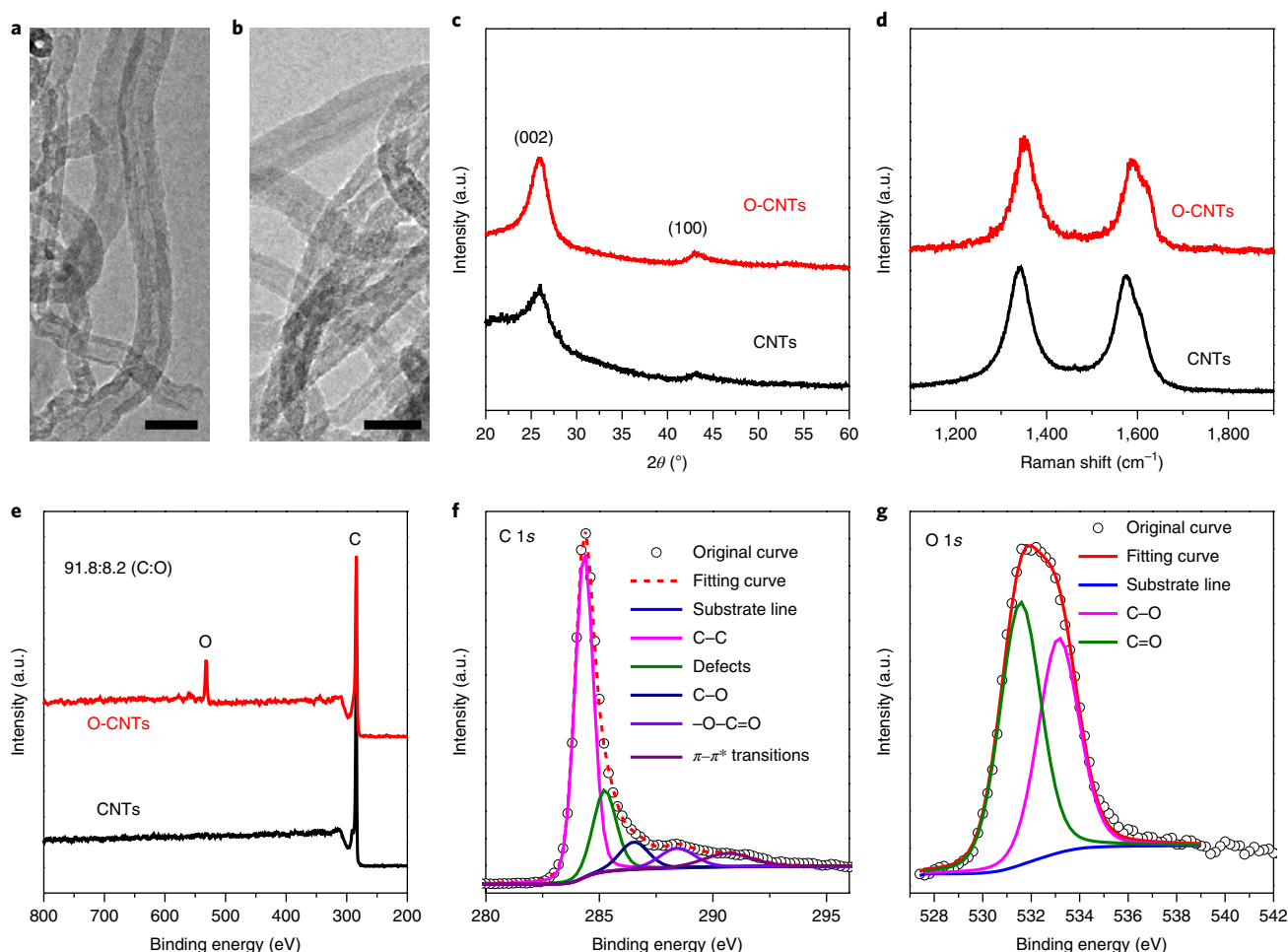


**Fig. 2 | Characterizations of CNTs and O-CNTs.** a, b, Transmission electron microscopy images of CNTs before (a) and after oxidation (b). Scale bars, 10 nm. c, d, X-ray diffraction patterns (c) and Raman spectra (d) of CNTs and O-CNTs. e, XPS survey of both samples. f, g, Deconvoluted carbon 1s (f) and oxygen 1s (g) spectra of O-CNTs. These results indicate that the oxidation treatment creates abundant oxygen-containing functional groups on the surface of CNTs.

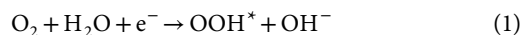
enhanced ORR performance (especially the onset potential) for O-SP, we can conclude that the presence of iron nanoparticles did not contribute substantially to ORR performance. Moreover, to mitigate the possible contribution from the iron, the commercial CNTs were first treated with concentrated HCl and NaSCN solution before performing ORR measurements. Electrochemical results demonstrated that the CNTs showed slightly enhanced ORR activity and  $\text{H}_2\text{O}_2$  selectivity before and after HCl and NaSCN treatment (Supplementary Fig. 6), further supporting our conclusion.

It has been reported that the defects in the carbon materials may act as reactive sites for oxygen adsorption or reduction during the electrocatalytic process<sup>25</sup>. In the present study, the O-CNTs were further treated in a mixed hydrogen/argon atmosphere to reduce the oxygen-containing functional group (R-O-CNTs). XPS data reveal that this hydrogen reduction process removed most of the oxygen while the R-O-CNT structure still retained defects, as shown by the Raman spectrum (Supplementary Fig. 7). However, in terms of ORR activity and selectivity, R-O-CNTs perform far worse than O-CNTs (Supplementary Fig. 8), indicating that oxygenated defects play an important role in these catalysts; for example, as active sites themselves or by affecting the electronic structure of the material.

**ORR activities of carbon nanoparticles and oxidized carbon nanoparticles.** The oxygen content on the catalysts can be tuned by changing the process time for oxidation. Longer oxidation times gave rise to a gradual increase in the oxygen content up to 9% within 48 h (Supplementary Fig. 9). In Fig. 3a,b, we have plotted the oxygen content of each sample versus the current and the selectivity at 0.6 V, respectively. A nearly linear correlation was

observed in both plots, further validating the importance of oxygen functional groups. To demonstrate the general efficacy of this surface oxidation strategy for the ORR to produce  $\text{H}_2\text{O}_2$ , we examined two other types of low-cost carbon material (SP and acetylene black (AB)) and found that the ORR activity and selectivity of the oxidized carbon materials (O-SP and O-AB; characterization shown in Supplementary Figs. 10–13) both improved significantly or were comparable in both basic and neutral electrolytes (Fig. 3c,d and Supplementary Figs. 14 and 15). Notably, O-SP and O-AB achieved selectivities of ~93 and ~72%, respectively, which are much higher than the values for original SP and AB (~68 and ~30%, respectively).

**DFT calculations.** The above experimental results demonstrate that the oxidation treatment of nanostructured carbons generates abundant oxygen functional groups, which may tailor the electronic structure of carbon materials and significantly modulate their oxygen reduction activity. The identification of active sites for this catalytic process is important for mechanistic understanding and for the rational design of future catalysts. Herein, we employ DFT calculations to study the activities of a wide range of oxygen functional groups (a total of nine configurations, as shown in Fig. 4a) towards ORR. A two-dimensional graphene sheet is used as the model system, where different types of oxygen functional groups, including carboxyl (–COOM, M=H and Na for this calculation), carbonyl (C=O), etheric (O–C–O) and hydroxyl (–OH) were introduced at different locations of the graphene; for example, the basal plane or edge. The activity of a catalyst for the ORR is determined to a large extent by its binding to all ORR intermediates ( $\text{OOH}^*$ , O and  $\text{OH}^*$ ). Thus, catalytic activities for the different structures are determined by the binding energies of the reaction intermediates to the active sites (the carbon atoms denoted by blue circles in Fig. 4a) of the catalyst. For the two-electron ORR, the overpotential is either due to hydrogenation of oxygen (equation (1)) or the reduction of  $\text{OOH}^*$  to form  $\text{H}_2\text{O}_2$  (equation (2)).



We use  $\Delta G_{\text{OOH}^*}$  as a descriptor and plot the activity volcano to underline the activities of different oxygen functional groups<sup>14,15</sup>. The limiting potential,  $U_L$ , which can be considered a metric of activity, is defined as the lowest potential at which all the reaction steps are downhill in free energy. The theoretical overpotential is defined as the maximum difference between the limiting potential and equilibrium potential. Figure 4b shows the calculated  $U_L$  as a function of  $\Delta G_{\text{OOH}^*}$  for the two-electron ORR to  $\text{H}_2\text{O}_2$  on these materials. The structures located on the right side of the volcano bind  $\text{OOH}^*$  weakly, hence equation (1) is a limiting step. Those located on the left side, however, bind  $\text{OOH}^*$  strongly, thus equation (2) is limiting. As a result, the binding strength of  $\text{OOH}^*$  to the surface ultimately determines the ORR activity. The maximum limiting potential is 0.70 V, representing zero overpotential at the top of the volcano. The computed values in Fig. 4 suggest that the –OH functional group does not significantly contribute to the ORR. However, the C–O–C groups on the basal plane and at the edge of the graphene (O basal 1 and O edge) are highly active for the two-electron reduction of oxygen to  $\text{H}_2\text{O}_2$  with overpotentials of 0.02 V and 0.06 V, respectively, comparable with the previously reported noble metal catalysts<sup>14</sup>. Among different possible configurations for the –COOM functional group, we find that the armchair edge is the most active (COOM edge 2), yielding an overpotential of 0.06 V.

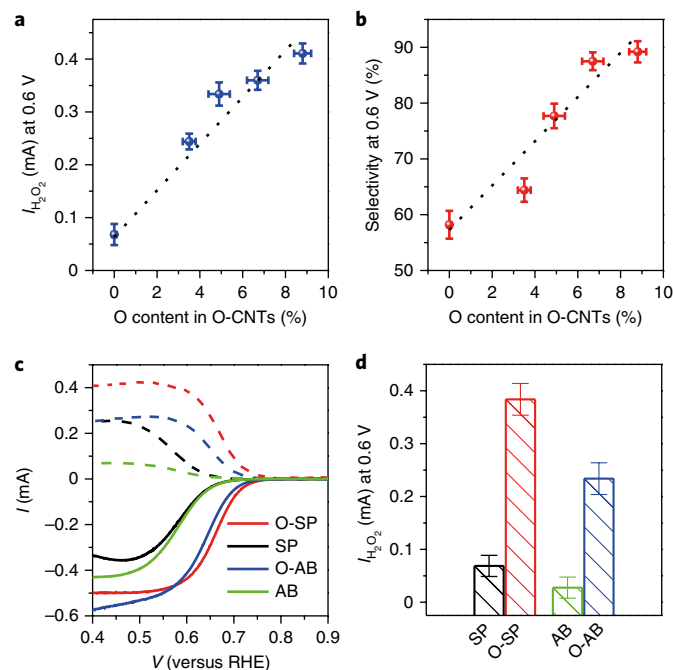


**Fig. 3 | ORR activities of O-CNTs with diverse oxygen content and other carbon materials.** **a,b**, Plots of  $\text{H}_2\text{O}_2$  current (**a**) and selectivity (**b**) at 0.6 V as a function of oxygen content for O-CNTs with various oxidation times, demonstrating that both the activity and selectivity correlate linearly with the oxygen content. **c**, Polarization curves at 1,600 r.p.m. (solid lines) and simultaneous  $\text{H}_2\text{O}_2$  detection currents at the ring electrode (dashed lines) for the carbon materials SP and AB and their oxidized derivatives. **d**,  $\text{H}_2\text{O}_2$  current (0.6 V) comparison of SP, O-SP, AB and O-AB, suggesting that the oxidation process is generally applicable for carbon materials.

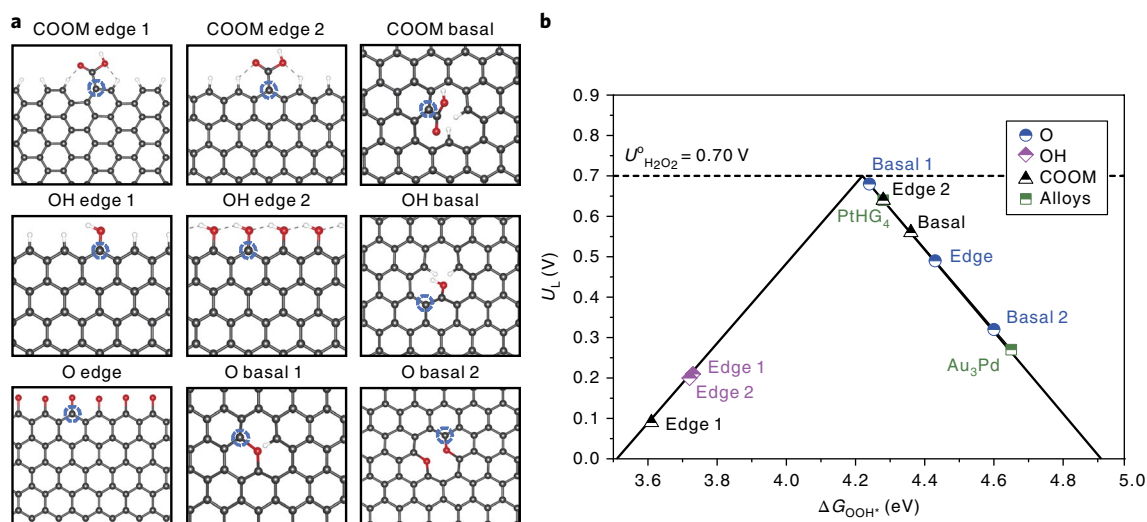


**Fig. 4 | DFT results of the ORR activities of different oxygen functional groups.** **a**, Different oxygen functional group type configurations examined in this study. The carbon atoms denoted by a blue circle are the active sites under investigation ( $M = \text{H}$  and  $\text{Na}$ ). **b**, Calculated two-electron (solid black) ORR-related volcano plot for the electro-reduction of oxygen to  $\text{H}_2\text{O}_2$  displayed with the limiting potential plotted as a function of  $\Delta G_{\text{OOH}^*}$ . The equilibrium potential for the two-electron ORR is shown as the dashed black line. The green squares display the activities of Pt-Hg and Pd-Au alloys adapted from ref. <sup>14</sup>, and the result for the OH basal configuration is out of the range.

## Discussion

While XPS analysis was helpful in elucidating the different species of oxidized carbon in these materials, the ratios were very similar in all the oxidized samples (Supplementary Table 4); thus, it is challenging to experimentally confirm the active functional groups unequivocally. Here, to support that the DFT results that demonstrate the oxygen functional groups ( $-\text{C}-\text{O}-\text{C}$  and  $-\text{COOM}$ ) are active and selective for electrochemical oxygen reduction to produce  $\text{H}_2\text{O}_2$ , we choose two different methods to fabricate O-CNTs, which are rich in these two functional groups. It should be noted that the nanotube morphologies are mostly preserved after these two oxidation methods (Supplementary Fig. 16), thus the possible contribution from morphology change to the overall ORR activity can be excluded. The first method is oxidizing CNTs by highly concentrated KOH solution at a high temperature (denoted by CNTs-KOH). According to the XPS results (Supplementary Fig. 17), the intensity of the  $\text{C}=\text{O}$  bond was much higher than that of the  $\text{C}-\text{O}$  bond, suggesting the formation of a  $-\text{COOH}$  functional group on the surface<sup>38</sup>. The broad peak at around 535 eV can be attributed to firmly adsorbed  $\text{H}_2\text{O}$ <sup>38</sup>. Thus, although the as-measured oxygen content is  $\sim 8.5\%$ , the oxygen content of the functional group should be much lower. The second method is oxidizing CNTs by mixing with poly(ethylene oxide) (PEO; mass ratio: 1:4) and carbonizing the mixture at 600 °C for 3 h (denoted by CNTs-PEO). The XPS results showed that the  $\text{C}-\text{O}$  bond was dominated in CNTs-PEO, indicating the formation of a  $-\text{C}-\text{O}-\text{C}$  functional group as the material was produced at a high temperature. The oxygen content was  $\sim 4.3\%$  for this material.

The electrochemical results reveal that both CNTs-KOH and CNTs-PEO show significantly improved ORR activity and selectivity ( $\sim 83\%$  and  $\sim 87\%$  for CNTs-KOH and CNTs-PEO, respectively), demonstrating that both functional groups are active sites for electrochemical reduction of oxygen to produce  $\text{H}_2\text{O}_2$ . Although the selectivity of both samples is comparable with O-CNTs, lower onset potentials are observed. We hypothesize that the different onset potentials can be attributed to the possibility of the presence of different oxygen functional groups. According to our DFT calculations, the type of functional group determines the activity. There also seems to be a synergy effect between different functional

groups. For example, the O-CNT catalyst shows multiple oxygen functional groups, thus it is possible that its activity may be affected by several highly active functional groups. As only one oxygen functional group is dominated in CNTs-KOH and CNTs-PEO, the possible synergistic effect seems to be negligible. Moreover, the CNTs-PEO shows slightly higher activity than CNTs-KOH, indicating that the  $-\text{C}-\text{O}-\text{C}$  functional group is more active than the  $-\text{COOM}$  group. Therefore, combined with our DFT calculation, we believe that the above results can further support the active sites of carbon materials for electrochemical  $\text{H}_2\text{O}_2$  synthesis. Overall, this combination of DFT calculations relating to the controlled synthesis of carbon materials with a variety of oxygen functional groups yields the fundamental understanding needed to provide guidance towards the design of future carbon-based catalysts for the electrochemical production of  $\text{H}_2\text{O}_2$ .

In summary, a surface oxidation treatment was shown to enhance the activity and selectivity of CNTs towards  $\text{H}_2\text{O}_2$  production by means of the ORR. The oxidized O-CNTs drastically lowered the needed overpotential by  $\sim 130$  mV at 0.2 mA compared with standard CNTs while simultaneously increasing the selectivity from  $\sim 60$  to  $\sim 90\%$ . The ORR activity and selectivity were also examined as a function of oxygen content in the O-CNTs and a nearly linear correlation emerged that reflects the importance of oxygen functional groups in driving catalysis. This surface oxidation approach was also effective for enhancing the ORR performance of other types of carbon material, validating the generality of this strategy. Based on DFT calculations, we can assign the origin of the high activity to the  $-\text{COOH}$  functional group in the armchair edge as well as the  $\text{C}-\text{O}-\text{C}$  functional group in the basal plane of the graphene, and these active functional groups are supported by further controlled experiments. We propose that our experimental observations, as well as the theoretical calculations, provide new insights into catalyst development that may be relevant in the production of industrial chemicals by means of clean, renewable electrical energy.

## Methods

**Surface oxidation of carbon materials.** First, the pre-determined quantities of raw CNTs (multiwalled, 0.2 g) and nitric acid (12 M, 200 ml) were added to a three-necked, round-bottomed glass flask. Afterwards, the reaction flask equipped with a reflux condenser, magnetic stirrer and thermometer was mounted in a preheated

water bath. The temperature was kept at 80 °C and the oxidized products were denoted by O-CNT-6, O-CNT-12, O-CNT-24 and O-CNT with oxidizing times of 6, 12, 24 and 48 h, respectively. After oxidation for a certain time, the slurry was taken out, cooled, centrifuged and washed with water and ethanol several times until the pH was neutral. Finally, the sample was dried at 60 °C in a vacuum oven overnight. For SP and AB, the oxidation process was similar to that for the CNTs (48 h). The reduction of O-CNTs was performed in a tube furnace at a temperature of 800 °C for 2 h under a mixed hydrogen (20%)/argon atmosphere.

**CNTs oxidized by other methods.** We chose two different methods to oxidize the CNTs to preferentially create different surface oxygen functional groups. One method was oxidizing CNTs by highly concentrated KOH solution in an autoclave. Briefly, ~50 mg of CNTs was first dispersed in 6 M KOH solution (40 ml). Afterwards, the suspension was transferred to an autoclave, which was sealed and put into an oven maintained at 180 °C for 12 h. After the reaction, the product was taken out, cooled down naturally, centrifuged and washed with water and ethanol several times until the pH was neutral. Finally, the sample was dried at 60 °C in a vacuum oven overnight. This product was denoted by CNTs-KOH. Another method was to oxidize the CNTs by mixing with PEO (mass ratio: 1:4) and carbonizing the mixture at 600 °C for 3 h under an argon atmosphere. This sample was denoted by CNTs-PEO.

**Characterization.** The size and morphology of the samples were measured using transmission electron microscopy (FEI Tecnai). XPS (SSI SProbe XPS spectrometer with Al(Kα) source) was used to determine the heteroatoms and functional groups. The X-ray powder diffraction patterns were recorded on an X-ray diffractometer (Rigaku D/max 2500) in the range 20–60°. The Raman and ultraviolet-visible spectroscopy were conducted in HORIBA Scientific LabRAM and Cary 6000i, respectively.

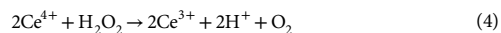
**Sample preparation and electrochemical characterization.** The electrodes were prepared by dispersing the oxidized products in ethanol to achieve a catalyst concentration of ~3.3 mg ml<sup>-1</sup> with 5 wt% Nafion. After sonication for 60 min, 6 μl of the catalyst ink was drop-dried onto a glassy carbon disc (area: 0.196 cm<sup>2</sup>). The electrochemical tests were performed in a computer-controlled Bio-Logic VSP Potentiostat with a three-electrode cell at room temperature. The glass carbon electrode loaded with catalyst was used as the working electrode. A graphite rod and a saturated calomel electrode were used as the counter and reference electrode, respectively. Two electrolytes with pH ~13 (0.1 M KOH) and ~7 (0.1 M phosphate buffered saline) were chosen. The ORR activity and selectivity were investigated by polarization curves and rotating ring-disk electrode measurements in oxygen-saturated electrolyte at a scan rate of 10 mV s<sup>-1</sup>. Polarization curves in nitrogen-saturated electrolytes were also recorded as a reference. Electrocatalytic H<sub>2</sub>O<sub>2</sub> production on Teflon-treated carbon fibre paper loaded with O-CNTs (~2 mg cm<sup>-2</sup>) was performed in a two-compartment cell with Nafion 117 membrane as separator. Both the cathode compartment (25 ml) and anode compartment were filled with the same electrolyte (1 M KOH). The polarization curves were both system resistance corrected.

H<sub>2</sub>O<sub>2</sub> selectivity of the O-CNTs on the rotating ring-disk electrode was calculated based on the current of both disc and ring electrodes (equation (3)). A potential of 1.2 V (versus the reversible hydrogen electrode) was applied on the ring of the working electrode at a speed of 1,600 r.p.m. during the entire testing process.

$$\text{H}_2\text{O}_2 \text{ yield: } \text{H}_2\text{O}_2(\%) = 200 \times \frac{I_{\text{R}}/N}{I_{\text{D}} + I_{\text{R}}/N} \quad (3)$$

where  $I_{\text{R}}$  is the ring current,  $I_{\text{D}}$  is the disk current and  $N$  is the collection efficiency (0.256 after calibration).

**H<sub>2</sub>O<sub>2</sub> concentration measurement.** The H<sub>2</sub>O<sub>2</sub> concentration was measured by a traditional cerium sulfate Ce(SO<sub>4</sub>)<sub>2</sub> titration method based on the mechanism that a yellow solution of Ce<sup>4+</sup> would be reduced by H<sub>2</sub>O<sub>2</sub> to colourless Ce<sup>3+</sup> (equation (4)). Thus, the concentration of Ce<sup>4+</sup> before and after the reaction can be measured by ultraviolet-visible spectroscopy. The wavelength used for the measurement was 316 nm.



Therefore, the concentration of H<sub>2</sub>O<sub>2</sub> ( $M$ ) can be determined by equation (5):

$$M = 2 \times M\text{Ce}^{4+} \quad (5)$$

where  $M\text{Ce}^{4+}$  is the mole of consumed Ce<sup>4+</sup>.

The yellow transparent Ce(SO<sub>4</sub>)<sub>2</sub> solution (1 mM) was prepared by dissolving 33.2 mg Ce(SO<sub>4</sub>)<sub>2</sub> in 100 ml 0.5 M sulfuric acid solution. To obtain the calibration curve, H<sub>2</sub>O<sub>2</sub> with known concentration was added to Ce(SO<sub>4</sub>)<sub>2</sub> solution and measured by ultraviolet-visible spectroscopy. Based on the linear relationship between the signal intensity and Ce<sup>4+</sup> concentration (~0.1–0.8 mM), the H<sub>2</sub>O<sub>2</sub> concentrations of the samples could be obtained. The concentration of H<sub>2</sub>O<sub>2</sub>

was also determined using commercially available H<sub>2</sub>O<sub>2</sub> testing strip paper. H<sub>2</sub>O<sub>2</sub> selectivity of the O-CNTs tested on Teflon-treated carbon fibre paper was determined by this method. The electrode was kept at the potential with an initial ORR current at ~20 mA cm<sup>-2</sup> until a certain amount of charge (10 C) was accumulated.

**Computational study.** The simulations were handled using the Atomic Simulation Environment<sup>39</sup>. The electronic structure calculations were performed using the QUANTUM ESPRESSO programme package<sup>40</sup>. The electronic wavefunctions were expanded in plane waves up to a cutoff energy of 500 eV, while the electron density was represented on a grid with an energy cutoff of 5,000 eV. Core electrons were approximated with ultrasoft pseudopotentials<sup>41</sup>. We used the BEEF-vdW exchange-correlation functional<sup>42</sup>, which has been shown to accurately describe chemisorption and physisorption properties on graphene. Graphene structures were modelled as one layer. A vacuum region of about 20 Å was used to decouple the periodic replicas. To model oxygen functional groups in the basal plane, we used a super cell of lateral size 8 × 8, and the Brillouin zone was sampled with (2 × 2 × 1) Monkhorst–Pack k-points. For the oxygen functional groups in the edge, we used the super cell of lateral size 3 × 4 and the Brillouin zone was sampled with (1 × 4 × 1) Monkhorst–Pack k-points.

**Details of the calculated free energy of adsorptions.** We considered three intermediates in the ORR: OH\*, O\* and OOH\*. The catalytic activity of the material was determined by the binding energies of the reaction intermediates to the active sites of the catalyst.

To estimate the adsorption energies of different intermediates at zero potential and pH = 0, we calculated the reaction energies of each individual intermediate and corrected them for zero-point energy (ZPE) and entropy (TS) using equation (6):

$$\Delta G = \Delta E + \Delta \text{ZPE} - T\Delta S \quad (6)$$

Additionally, we used the computational hydrogen electrode model, which exploits the fact that the chemical potential of a proton–electron pair is equal to gas-phase hydrogen at standard conditions, and the electrode potential was taken into account by shifting the electron energy by  $-eU$  where  $e$  and  $U$  are the elementary charge and the electrode potential, respectively<sup>43</sup>. As the ground state of the oxygen and H<sub>2</sub>O<sub>2</sub> molecules are poorly described in DFT calculations, we used gas-phase H<sub>2</sub>O and hydrogen as reference states as they are readily treated in the DFT calculations. The entropy for H<sub>2</sub>O was calculated at 0.035 bar, which is the equilibrium pressure of H<sub>2</sub>O at 300 K. The free energy of this state is therefore equal to that of liquid water<sup>43</sup>.

**Data availability.** The data that support the plots within this paper and other findings of this study are available from the corresponding author upon reasonable request.

Received: 10 June 2017; Accepted: 1 December 2017;

Published online: 15 January 2018

## References

- Myers, R. L. *The 100 Most Important Chemical Compounds* (Greenwood Press, London, 2007).
- Fukuzumi, S., Yamada, Y. & Karlin, K. D. Hydrogen peroxide as a sustainable energy carrier: electrocatalytic production of hydrogen peroxide and the fuel cell. *Electrochim. Acta* **82**, 493–511 (2012).
- Campos-Martin, J. M., Blanco-Brieva, G. & Fierro, J. L. Hydrogen peroxide synthesis: an outlook beyond the anthraquinone process. *Angew. Chem. Int. Ed.* **45**, 6962–6984 (2006).
- Edwards, J. K. et al. Switching off hydrogen peroxide hydrogenation in the direct synthesis process. *Science* **323**, 1037–1041 (2009).
- Solsona, B. E. et al. Direct synthesis of hydrogen peroxide from H<sub>2</sub> and O<sub>2</sub> using Al<sub>2</sub>O<sub>3</sub> supported Au–Pd catalysts. *Chem. Mater.* **18**, 2689–2695 (2006).
- Freakley, S. J. et al. Palladium–tin catalysts for the direct synthesis of H<sub>2</sub>O<sub>2</sub> with high selectivity. *Science* **351**, 965–968 (2016).
- Samanta, C. Direct synthesis of hydrogen peroxide from hydrogen and oxygen: an overview of recent developments in the process. *Appl. Catal. A Gen.* **350**, 133–149 (2008).
- Edwards, J. K., Freakley, S. J., Lewis, R. J., Pritchard, J. C. & Hutchings, G. J. Advances in the direct synthesis of hydrogen peroxide from hydrogen and oxygen. *Catal. Today* **248**, 3–9 (2015).
- Rankin, R. B. & Greeley, J. Trends in selective hydrogen peroxide production on transition metal surfaces from first principles. *ACS Catal.* **2**, 2664–2672 (2012).
- Solsona, B. E. et al. Direct synthesis of hydrogen peroxide from H<sub>2</sub> and O<sub>2</sub> using Al<sub>2</sub>O<sub>3</sub> supported Au–Pd catalysts. *Chem. Mater.* **18**, 2689–2695 (2006).
- Wood, K. N., O’Hayre, R. & Pylypenko, S. Recent progress on nitrogen/carbon structures designed for use in energy and sustainability applications. *Energy Environ. Sci.* **7**, 1212–1249 (2014).

12. Drogui, P., Elmaleh, S., Rumeau, M., Bernard, C. & Rambaud, A. Hydrogen peroxide production by water electrolysis: application to disinfection. *J. Appl. Electrochem.* **31**, 877–882 (2001).
13. Yamanaka, I. & Murayama, T. Neutral H<sub>2</sub>O<sub>2</sub> synthesis by electrolysis of water and O<sub>2</sub>. *Angew. Chem. Int. Ed.* **47**, 1900–1902 (2008).
14. Siahrostami, S. et al. Enabling direct H<sub>2</sub>O<sub>2</sub> production through rational electrocatalyst design. *Nat. Mater.* **12**, 1137–1143 (2013).
15. Verdaguier-Casadevall, A. et al. Trends in the electrochemical synthesis of H<sub>2</sub>O<sub>2</sub>: enhancing activity and selectivity by electrocatalytic site engineering. *Nano Lett.* **14**, 1603–1608 (2014).
16. Fellingner, T.-P., Hasché, F., Strasser, P. & Antonietti, M. Mesoporous nitrogen-doped carbon for the electrocatalytic synthesis of hydrogen peroxide. *J. Am. Chem. Soc.* **134**, 4072–4075 (2012).
17. Choi, C. H. et al. Hydrogen peroxide synthesis via enhanced two-electron oxygen reduction pathway on carbon-coated Pt surface. *J. Phys. Chem. C* **118**, 30063–30070 (2014).
18. Park, J., Nabae, Y., Hayakawa, T. & Kakimoto, M. Highly selective two-electron oxygen reduction catalyzed by mesoporous nitrogen-doped carbon. *ACS Catal.* **4**, 3749–3754 (2014).
19. Choi, C. H. et al. Tuning selectivity of electrochemical reactions by atomically dispersed platinum catalyst. *Nat. Commun.* **7**, 10922 (2016).
20. Chen, Z. et al. Development of a reactor with carbon catalysts for modular-scale, low-cost electrochemical generation of H<sub>2</sub>O<sub>2</sub>. *React. Chem. Eng.* **2**, 239–245 (2017).
21. Jirkovský, J. S. et al. Single atom hot-spots at Au–Pd nanoalloys for electrocatalytic H<sub>2</sub>O<sub>2</sub> production. *J. Am. Chem. Soc.* **133**, 19432–19441 (2011).
22. Perazzolo, V. et al. Nitrogen and sulfur doped mesoporous carbon as metal-free electrocatalysts for the in situ production of hydrogen peroxide. *Carbon* **95**, 949–963 (2015).
23. Sidik, R. A., Anderson, A. B., Subramanian, N. P., Kumaraguru, S. P. & Popov, B. N. O<sub>2</sub> reduction on graphite and nitrogen-doped graphite: experiment and theory. *J. Phys. Chem. B* **110**, 1787–1793 (2006).
24. Hasché, F., Oezaslan, M., Strasser, P. & Fellingner, T.-P. Electrocatalytic hydrogen peroxide formation on mesoporous non-metal nitrogen-doped carbon catalyst. *J. Energy Chem.* **25**, 251–257 (2016).
25. Liu, Y., Quan, X., Fan, X., Wang, H. & Chen, S. High-yield electrosynthesis of hydrogen peroxide from oxygen reduction by hierarchically porous carbon. *Angew. Chem. Int. Ed.* **54**, 6837–6841 (2015).
26. Li, N. et al. A novel carbon black graphite hybrid air-cathode for efficient hydrogen peroxide production in bioelectrochemical systems. *J. Power Sources* **306**, 495–502 (2016).
27. Moraes, A. et al. Surface and catalytic effects on treated carbon materials for hydrogen peroxide electrogeneration. *Electrocatalysis* **7**, 60–69 (2016).
28. Rosca, I. D., Watari, F., Uo, M. & Akasaka, T. Oxidation of multiwalled carbon nanotubes by nitric acid. *Carbon* **43**, 3124–3131 (2005).
29. Liang, Y. et al. Co<sub>3</sub>O<sub>4</sub> nanocrystals on graphene as a synergistic catalyst for oxygen reduction reaction. *Nat. Mater.* **10**, 780–786 (2011).
30. Assumpção, M. et al. A comparative study of the electrogeneration of hydrogen peroxide using Vulcan and Printex carbon supports. *Carbon* **49**, 2842–2851 (2011).
31. Barros, W. R. Oxygen reduction to hydrogen peroxide on Fe<sub>3</sub>O<sub>4</sub> nanoparticles supported on Printex carbon and graphene. *Electrochim. Acta* **162**, 263–270 (2015).
32. Mehta, V. & Cooper, J. S. Review and analysis of PEM fuel cell design and manufacturing. *J. Power Sources* **114**, 32–53 (2003).
33. Lu, Z. Superaerophilic carbon-nanotube-array electrode for high-performance oxygen reduction reaction. *Adv. Mater.* **28**, 7155–7161 (2016).
34. Datsyuk, V. et al. Chemical oxidation of multiwalled carbon nanotubes. *Carbon* **46**, 833–840 (2008).
35. Kundu, S., Wang, Y., Xia, W. & Muhler, M. Thermal stability and reducibility of oxygen-containing functional groups on multiwalled carbon nanotube surfaces: a quantitative high-resolution XPS and TPD/TPR study. *J. Phys. Chem. C* **112**, 16869–16878 (2008).
36. Andrews, R., Jacques, D., Qian, D. & Rantell, T. Multiwall carbon nanotubes: synthesis and application. *Acc. Chem. Res.* **35**, 1008–1017 (2002).
37. Huang, W., Wang, Y., Luo, G. & Wei, F. 99.9% purity multi-walled carbon nanotubes by vacuum high-temperature annealing. *Carbon* **41**, 2585–2590 (2003).
38. Yue, Z., Jiang, W., Wang, L., Gardner, S. & Pittman, C. U. Surface characterization of electrochemically oxidized carbon fibers. *Carbon* **37**, 1785–1796 (1999).
39. Bahn, S. R. & Jacobsen, K. W. An object-oriented scripting interface to a legacy electronic structure code. *Comput. Sci. Eng.* **4**, 56–66 (2002).
40. Giannozzi, P. et al. QUANTUM ESPRESSO: a modular and open-source software project for quantum simulations of materials. *J. Phys. Condens. Matter* **21**, 395502 (2009).
41. Adllan, A. A. & Dal Corso, A. Ultrasoft pseudopotentials and projector augmented-wave data sets: application to diatomic molecules. *J. Phys. Condens. Matter* **23**, 425501 (2011).
42. Wellendorff, J. et al. Density functionals for surface science: exchange-correlation model development with Bayesian error estimation. *Phys. Rev. B* **85**, 235149 (2012).
43. Nørskov, J. K. et al. Origin of the overpotential for oxygen reduction at a fuel-cell cathode. *J. Phys. Chem. B* **108**, 17886–17892 (2004).

### Acknowledgements

This work was initiated by the support of the Materials Sciences and Engineering Division of the Basic Energy Sciences office at the US Department of Energy, under contract DEAC02-76-SFO0515. We acknowledge support from SUNCAT seed funding in SLAC. We also gratefully acknowledge support from the Chemical Sciences, Geosciences, and Biosciences Division of the Office of Sciences at the US Department of Energy to the SUNCAT Center for Interface Science and Catalysis under award number DE-SC0004993.

### Author contributions

Z.L., G.C., S.S. and Y.C. conceived the research. Z.L., G.C., Z.C., K.L., J.X., L.L., T.W., D.L. and Y.L. performed the experiments. S.S. and J.K.N. performed the theoretical calculation. Z.L., G.C., Z.C., T.F.J. and Y.C. contributed new reagents and analytical tools. Z.L., G.C., S.S., Z.C., T.F.J., J.K.N. and Y.C. analysed the data. Z.L., G.C., S.S., Z.C., T.F.J., J.K.N. and Y.C. wrote the paper.

### Competing interests

The authors declare no competing financial interests.

### Additional information

**Supplementary information** is available for this paper at <https://doi.org/10.1038/s41929-017-0017-x>.

**Reprints and permissions information** is available at [www.nature.com/reprints](http://www.nature.com/reprints).

**Correspondence and requests for materials** should be addressed to Y.C.

**Publisher's note:** Springer Nature remains neutral with regard to jurisdictional claims in published maps and institutional affiliations.